Supporting information

Interactions between CO oxidation and selective catalytic reduction of NO with NH_3 over Mn-based catalysts

Liyan Wang[1, §], Bin wang[1, 2,§], Yangyang Guo[2], Yang Zheng[2], Tingyu Zhu[2,3*]*

[1]School of Chemical & Environmental Engineering, China University of Mining & Technology, Beijing 100083, China

[2]Beijing Engineering Research Centre of Process Pollution Control, National Engineering Laboratory for Hydrometallurgical Cleaner Production Technology, Institute of Process Engineering, Chinese Academy of Sciences, Beijing 100190, China

[3]Center for Excellence in Regional Atmospheric Environment, Institute of Urban Environment, Chinese Academy of Sciences, Xiamen 361021, China

[§]Liyan Wang and Bin Wang contributed equally to this work.

*To whom correspondence should be addressed

Y. Guo, Institute of Process Engineering, Chinese Academy of Sciences, Beijing 100190, China

Tel. /fax: +86-10-82544823 Email: yyguo@ipe.ac.cn

T. Zhu, Institute of Process Engineering, Chinese Academy of Sciences, Beijing 100190, China

Tel. /fax: +86-10-82544821 Email: tyzhu@ipe.ac.cn

1. The N_2 selectivity of α-r and α-r-M (M=Fe, Co, Ce Cu) catalysts

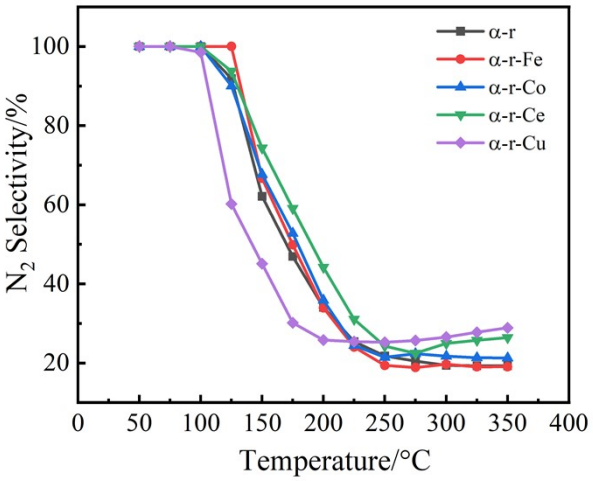

Fig. S1 N_2 selectivity of α-r and α-r-M (M=Fe, Co, Ce, Cu) catalysts.

Reaction conditions: [NH_3]=500 ppm, [NO]=500 ppm, [CO]=5000 ppm, [O_2]=5%, balanced N_2

2. Activity evaluation and byproduct distribution of NH_3-SCO over α-r-Cu catalyst

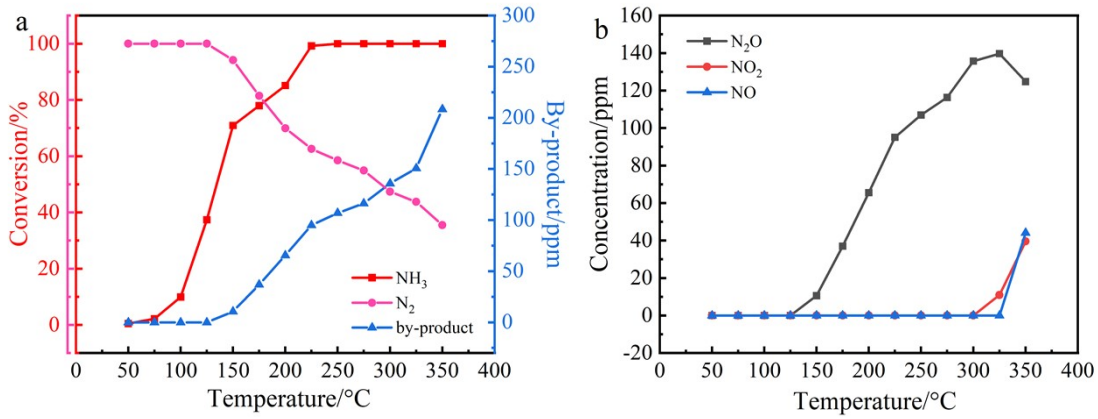

Fig. S2 Activity evaluation (a) and byproduct distribution (b) of NH_3-SCO over the α-r-Cu catalyst. Reaction conditions: [NH_3]=500 ppm, [O_2]=5%, balanced N_2.

NH_3 was almost completely transformed, and N_2 selectivity reached 62.5% at 225°C.

=

3. Activity evaluation and byproduct distribution of CO-SCR over α-r-Cu catalyst

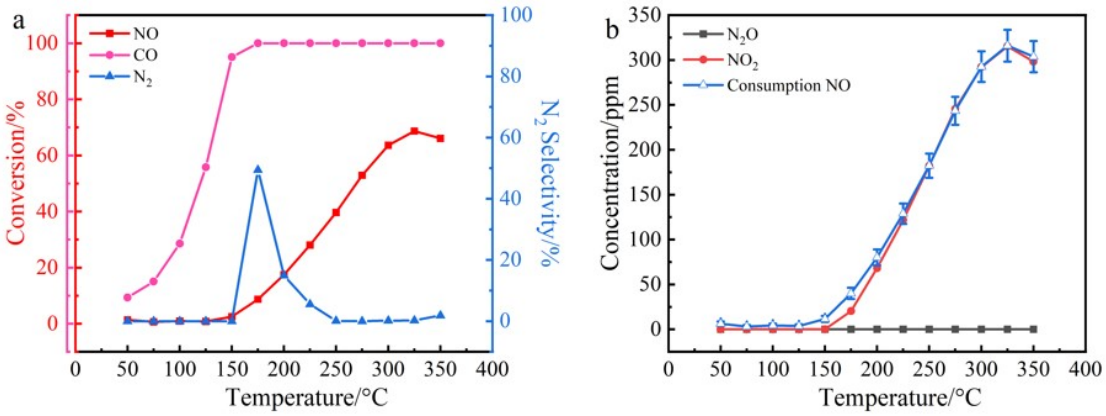

Fig. S3 Activity evaluation (a) and byproduct distribution (b) of CO-SCR over α-r-Cu catalyst. Reaction conditions: [CO]=5000 ppm, [NO]=500 ppm, [O_2]=5%, balanced N_2.

NO could not be completely converted over the whole temperature range, and the selectivity decreased with temperature, while CO conversion reached 100% at 175°C. In addition, the consumed NO was almost completely transformed into NO_2, indicating that under oxygen-rich conditions, CO and O_2 reacted completely to generate CO_2, and NO reacted with O_2 to generate NO_2.

4. Comparison of total byproducts on α-r-Cu catalyst

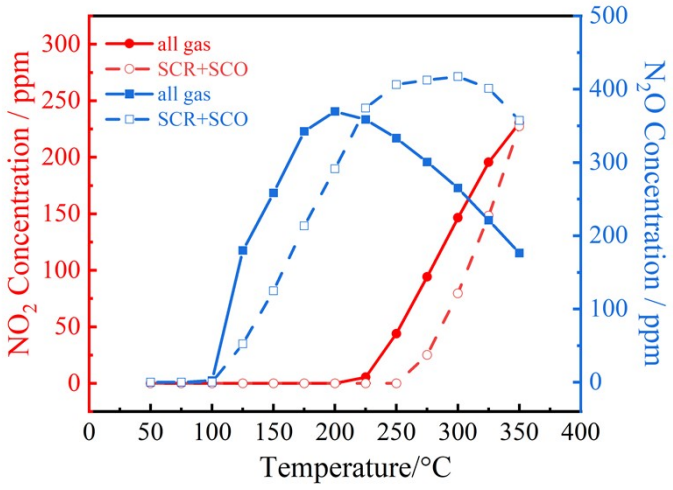

Fig. S4 Comparison of the sum of the byproducts of the SCR reaction and the SCO reaction with the total byproducts of the reaction in all gas atmosphere over the α-r-Cu catalyst. Reaction conditions: [NH_3]=500 ppm, [NO]=500 ppm, [CO]=5000 ppm, [O_2]=5%, balanced N_2.

5. The SEM and EDS images of α-r, α-r-Fe, α-r-Co, α-r-Ce and α-r-Cu catalysts

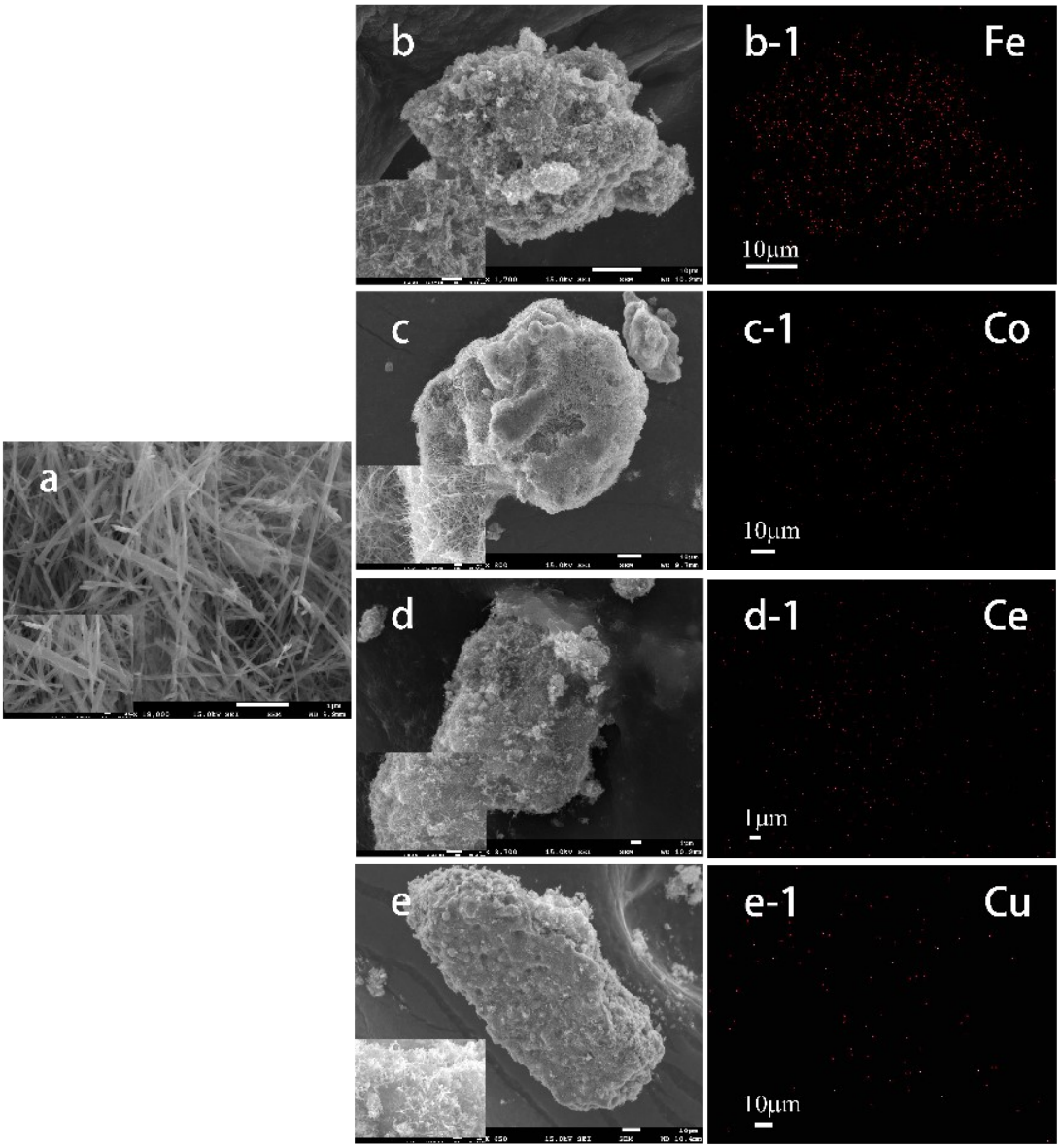

Fig. S5 SEM images of the α-r (a), α-r-Fe (b), α-r-Co (c), α-r-Ce (d) and α-r-Cu (e) catalysts and EDS images of α-r-Fe (b-1), α-r-Co (c-1), α-r-Ce (d-1) and α-r-Cu (e-1) catalysts

6. The BJH pore size distribution of α-r and α-r-M (M=Fe, Co, Ce, Cu) catalysts

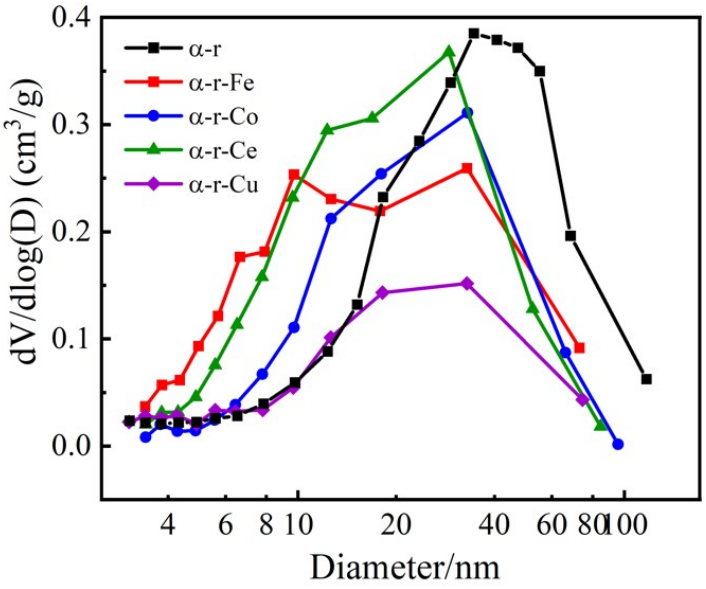

Fig. S6 The BJH pore size distribution of α-r and α-r-M (M=Fe, Co, Ce, Cu) catalysts.

7. The initial H_2 consumption rate of α-r and α-r-M (M=Fe, Co, Ce, Cu) catalysts

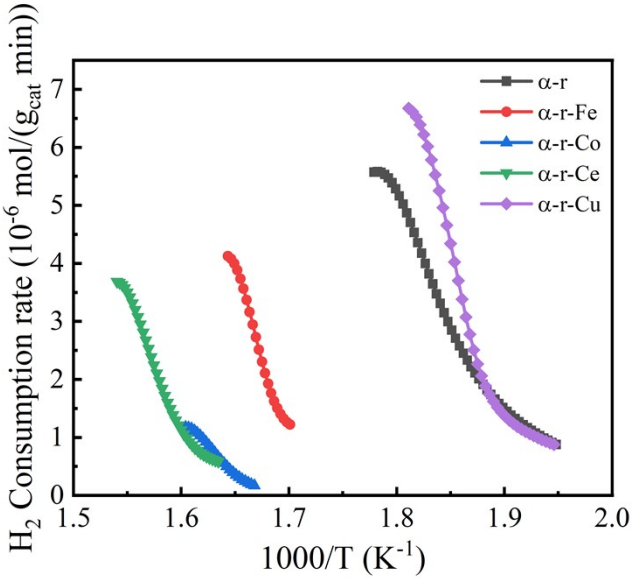

Fig. S7 The initial H_2 consumption rate of α-r and α-r-M (M=Fe, Co, Ce, Cu) catalysts.

8. Individual adsorption and desorption of NH_3, NO and CO

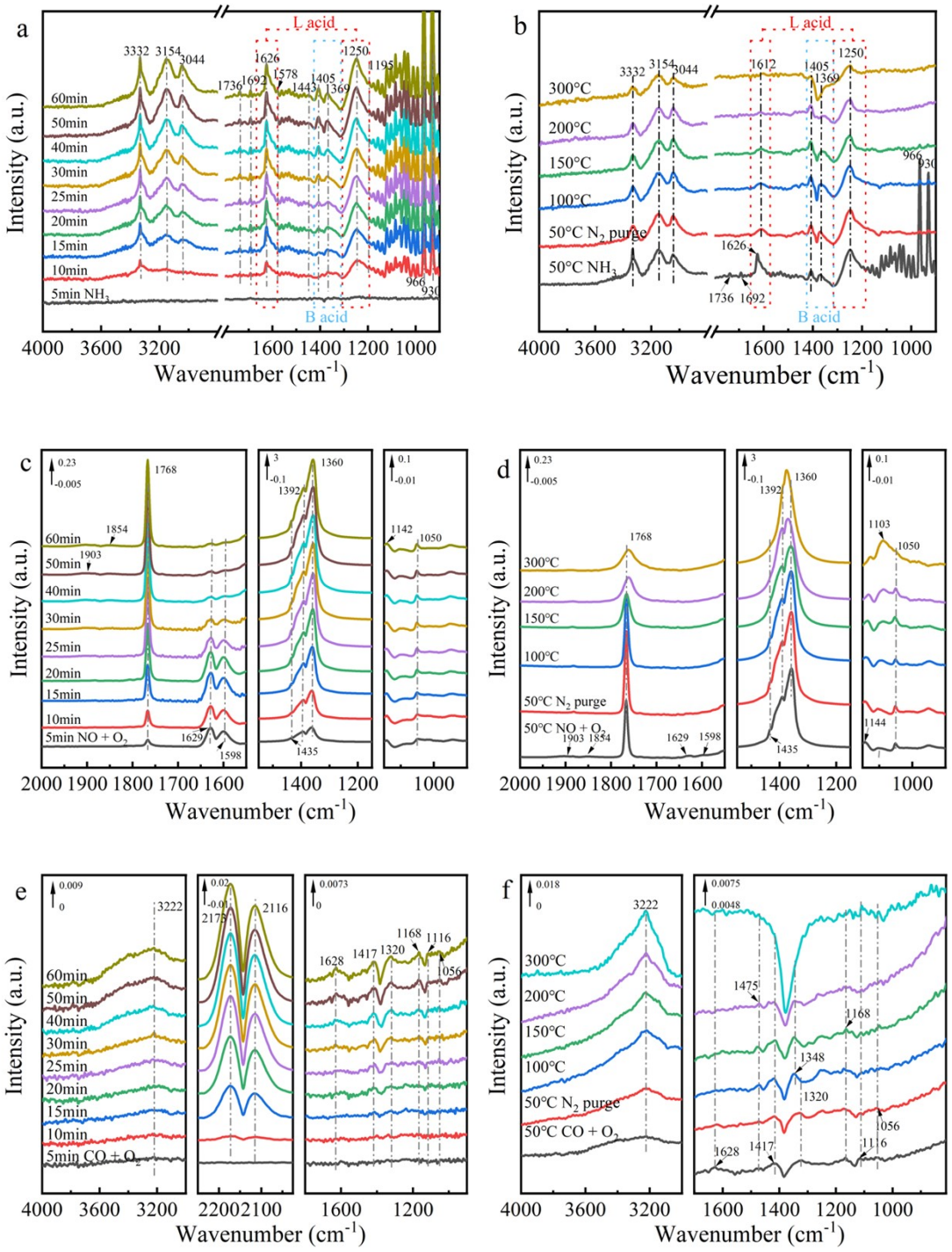

Fig. S8 *In situ* DRIFT spectra of NH_3(a), $NO+O_2$(c), CO (e) adsorption at 50°C and NH_3(b), $NO+O_2$(d), CO (f) desorption from 50-300°C over the α-r-Cu catalyst.

Reaction conditions: $[NH_3]$=1000 ppm, [NO]=1000 ppm, [CO]=5000 ppm, $[O_2]$=5%, balanced N_2

The adsorption and desorption behaviors of NH_3, NO + O_2 and CO on the α-r-Cu catalyst were investigated by *in situ* DRIFT spectroscopy. *In situ* DRIFT spectra of

NH_3 absorption and desorption are shown in Fig. S8a and Fig. S8b, and the peak attribution is concluded in Table S3. It has been reported that ionic NH_4^+ and coordination NH_3 can participate in the SCR process by reacting with NO_2 adsorbed species to form active intermediates [1]. The intensity of all the peaks increases with time. Under N_2 purging at 50°C, the peaks of NH_3 at 1736 and 1692 cm^{-1} and the peaks at 966 and 930 cm^{-1} gradually disappeared, indicating that the two peaks belong to the peaks of symmetric stretching vibration and gaseous NH_3. The intensity of all peaks decreased significantly with increasing temperature. The peak at 1626 cm^{-1} was obviously weakened under N_2 purge at 50°C, and disappeared when the temperature rose to 100°C, reflecting that the peak is asymmetric bending vibration peaks of gaseous and physical adsorbed state NH_3 belonging to L acid. The symmetrical bending vibration peaks of NH_3 and weak chemisorbed NH_3 at 1176-1130 cm^{-1} gradually disappeared under N_2 purge, and the peaks disappeared when the temperature rose to 150°C. When the temperature rose to 200°C, the peak of coordinated NH_3 on the Lewis acid sites at 1605 cm^{-1} gradually disappeared. These peaks are mainly weak acid sites according to Fig. 5c. When the temperature rose to 300°C, NH_4^+ on Brønsted acid sitess at 1405 and 1369 cm^{-1} gradually disappeared. Meanwhile, only L acid and a small amount of B acid remained when the temperature rose to 300°C. As a result, the coordinated NH_3 on Lewis acid sitess is much more stable than NH_4^+ ions on Brønsted acid sitess at high temperatures.

In situ DRIFT spectra of NO + O_2 absorption and desorption at different temperatures of the α-r-Cu catalyst are shown in Fig. S8c and Fig. S8d. With increasing NO + O_2 penetration time, the α-r-Cu catalyst gradually exhibited thirteen peaks at 1903, 1854, 1882, 1768, 1629, 1598, 1435, 1392, 1360, 1144, 1103, 1050 and 833 cm^{-1} (Table S4). Under N_2 purge at 50°C, the bending vibration peaks of gaseous and physically adsorbed NO at 1903 and 1854 cm^{-1} gradually disappeared, while the asymmetric bending vibration peaks of gaseous and physically adsorbed NO_2 at 1629 and 1598 cm^{-1} decreased significantly and disappeared when increased to 100°C. In addition, the stretching vibration peaks of dinitrosyl species at 1882 and 1768 cm^{-1} decreased significantly with increasing temperature. When the temperature increased

to 100°C, the intensity of bidentate nitrate at 1360 cm^{-1} decreased and blueshifted at 200°C. This result indicated that nitrosyl and nitrite species are easily decomposed by heat. When the temperature was raised to 300°C, the peak of monodentate nitrite at 1435 cm^{-1} decreased and disappeared significantly, and the asymmetric stretching vibration peak of trans-$(N_2O_2)^{2-}$ at 1103 cm^{-1} was redshifted and significantly enhanced, indicating that high temperature was beneficial to the formation of the species. Furthermore, the peak intensity of monodentate nitrate at 1392 cm^{-1} began to increase at 200°C, and redshifted to 1375 cm^{-1}, indicating that monodentate nitrate began to be decomposed at 200°C. Combined with NO-TPD, it can be seen that the intermediate species adsorbed by NO + O_2 mainly existed in the form of nitrate.

In situ DRIFT spectra of CO absorption and desorption at different temperatures of the α-r-Cu catalyst are shown in Fig. S8e, S8f and Table S5. Under N_2 purging at 50°C, the bending vibration peaks of gaseous and physical adsorbed CO at 2173 and 2116 cm^{-1} gradually disappeared. The intensity of the asymmetric and symmetric stretching vibration peaks of HCO_3^- at 1628 and 1417cm^{-1} gradually decreased with increasing temperature and almost disappeared at 200°C, indicating that HCO_3^- species are easily decomposed by heat. When the temperature rose to 100°C, the asymmetric stretching vibration peak of unidentate carbonate at 1475 cm^{-1} appeared, reflecting that HCO_3^- species decomposed to produce the carbonate species. Meanwhile, the stretching vibration peak of bidentate carbonate at 1320 cm^{-1} disappeared, and unidentate carbonate at 1348 cm^{-1} gradually increased, indicating that bidentate carbonate decomposes into unidentate carbonate with increasing temperature.

Table S1 The integral area of O_2-TPD over α-r-M (M=Fe, Co, Ce, Cu) catalysts

Material	Area of Peak I	Area of Peak II (a.u.)	Area of Peak III (a.u.)	Total oxygen storage (a.u.)
α-r	/	2.628E-9	1.005E-9	3.633E-9
α-r-Fe	/	2.800E-9	4.009E-10	3.201E-9
α-r-Co	/	2.637E-9	9.878E-10	3.625E-9
α-r-Ce	/	2.941E-9	2.072E-10	3.148E-9
α-r-Cu	/	2.926E-9	8.217E-10	3.748E-9

Table S2 The integral area of NH_3-TPD over α-r and α-r-M (M=Fe, Co, Ce, Cu) catalysts

Material	Area of Peak I (a.u.)	Area of Peak II (a.u.)	Area of Peak III (a.u.)	Total (a.u.)	Area of Peak I + III (a.u.)
α-r	11	19	135	165	146
α-r-Fe	21	38	179	238	200
α-r-Co	20	24	163	207	183
α-r-Ce	34	63	128	225	162
α-r-Cu	15	23	216	254	231

Table S3 Data related to infrared study of NH_3 adsorption

Wavenumber/cm^{-1}	Attribution judgment	Reference
3332, 3154, 3044	N—H stretching vibration peak of coordinate NH_3	2
1736, 1692	Symmetric stretching vibration peak of NH_3	
1626	Asymmetric bending vibration peaks of gaseous and physically adsorbed NH_3 on Lewis acid	
1605, 1195	Asymmetric and symmetric N—H bending vibration peak peak of coordinate NH_3 on Lewis acid	3, 4
1595	Asymmetric bending vibration peaks of NH_3 coordination on Lewis acid	5, 6
1405, 1369	Symmetric bending vibration peaks of NH_4^+ on Brønsted acid	3, 7
1578-1443	Bending vibration peaks of —NH_2 and N—H	2, 8
1346-1320	Wagging bending vibration peak of —NH_2 on N_2H_4	8
1250	Symmetric N—H stretching vibration peak peak of coordinate NH_3 on Lewis acid	3, 9
1176-1130	Symmetric bending vibrations of NH_3 and weakly chemisorbed NH_3	10
1130—990	Wagging bending vibration peak of NH_3	

966, 930	Gaseous NH_3 peak

Table S4 Data related to infrared study of NO adsorpti**on**

Wavenumber/cm^{-1}	Attribution judgment	Reference
1903, 1854	Bending vibration peaks of gaseous and physically adsorbed NO	
1882, 1768	Stretching vibration peak of dinitrosyl species	11
1629, 1598	Asymmetric bending vibration peaks of gaseous and physically adsorbed NO_2	12
1435	Stretching vibration peak of N=O in monodentate nitrite	
1392	Stretching vibration peak of monodentate nitrate	13
1360	Stretching vibration peak of bidentate nitrate	14
1144	Stretching vibration peak of nitrite	
1103	Asymmetric Stretching vibration peaks of trans-$(N_2O_2)^{2-}$	15
1050	Bending vibration peaks of surface nitro compounds	3
833	Stable nitrate or nitrite	

Table S5 Data related to infrared study of CO adsorption

Wavenumber/cm^{-1}	Attribution judgment	Reference
3222	—OH	
2173, 2116	Bending vibration peaks of gaseous and physically adsorbed CO	
1628, 1417	Asymmetric and symmetric stretching vibration peak of HCO_3^-	16
1475, 1348	Asymmetric stretching vibration and symmetric stretching vibration peaks of unidentate carbonate	16
1320	Stretching vibration peaks of bidentate carbonate	17
1250	Stretching vibration peaks of carbonate	18
1168	Stretching vibration peaks of bridge carbonate	
1116, 1056	Peaks of carbonate and inorganic carboxylate	19

In Fig. 7a, the bending vibration peaks of gaseous and physically adsorbed NO at 1903 and 1854 cm^{-1} and the asymmetric bending vibration peaks of gaseous and physically adsorbed NO_2 at 1629 and 1598cm^{-1} gradually disappeared. With the introduction of NH_3, the asymmetric bending vibration peaks of gaseous and physically adsorbed NH_3 on L acid at 1626 cm^{-1} gradually appeared, and the peak of coordinate NH_3 on L acid at 1250 cm^{-1} gradually increased.

In Fig. 7b, the bending vibration peaks of gaseous and physically adsorbed NO at 1903 and 1854 cm^{-1} gradually appeared, while the stretching vibration peak of the dinitrosyl species at 1768 cm^{-1} did not appear, and the asymmetric bending vibration peaks of the gaseous and physically adsorbed NO_2 at 1629 and 1598 cm^{-1} were significantly enhanced.

In Fig. 8b, after NO + O_2 was introduced, the asymmetric stretching vibration peaks of Mn-COO formate at 1588 and 1562 cm^{-1} gradually disappeared, and the stretching vibration peak of bridge carbonate at 1168 cm^{-1} disappeared. The symmetrical stretching vibration peak of inorganic carboxylate at 1056 cm^{-1} disappeared, and the peaks of gaseous and physically adsorbed CO at 2173 and 2116 cm^{-1} gradually disappeared

Reference

1. F. Liu, H. He, Y. Ding and C. Zhang, *Appl. Catal. B: Environ.*, 2009, **93**, 194-204.
2. Y. Zhang, X. Zhao, H. Xu, K. Shen, C. Zhou, B. Jin and K. Sun, *J. Colloid Interface Sci.*, 2011, **361**, 212-218.
3. Z. Si, D. Weng, X. Wu, J. Li and G. Li, *J. Catal.*, 2010, **271**, 43-51.
4. L. Chen, Z. Si, X. Wu and D. Weng, *ACS Appl. Mater. Interfaces*, 2014, **6**, 8134-8145.
5. Q. Yan, S. Chen, C. Zhang, Q. Wang and B. Louis, *Appl. Catal. B: Environ.*, 2018, **238**, 236-247.
6. M. Guo, P. Zhao, Q. Liu, C. Liu, J. Han, N. Ji, C. Song, D. Ma, X. Lu, X. Liang and Z. Li, *ChemCatChem*, 2019, **11**, 4954-4965.
7. F. Liu and H. He, *Catal. Today*, 2010, **153**, 70-76.
8. X. Wu, W. Yu, Z. Si and D. Weng, *Front. Env. Sci. Eng.*, 2013, **7**, 420-427.
9. Z. Liu, Y. Liu, Y. Li, H. Su and L. Ma, *Chem. Eng. J.*, 2016, **283**, 1044-1050.
10. Z. Liu, J. Zhu, J. Li, L. Ma and S. I. Woo, *ACS Appl. Mater. Interfaces*, 2014, **6**, 14500-14508.
11. M. A. Centeno, I. Carrizosa and J. A. Odriozola, *Appl. Catal. B: Environ.*, 2001, **29**, 307-314.

12. Y. Wang, C. Ge, L. Zhan, C. Li, W. Qiao and L. Ling, *Ind. Eng. Chem. Res.*, 2012, **51**, 11667-11673.
13. Y. Li, Y. Li, P. Wang, W. Hu, S. Zhang, Q. Shi and S. Zhan, *Chem. Eng. J.*, 2017, **330**, 213-222.
14. S. Roy, M. S. Hegde and G. Madras, *Appl. Energy*, 2009, **86**, 2283-2297.
15. A. Martínez-Arias, J. Soria, J. C. Conesa, X. L. Seoane, A. Arcoya and R. Cataluña, *J. Chem. Soc., Faraday Trans.*, 1995, **91**, 1679-1687.
16. Y. Lang, J. Zhang, Z. Feng, X. Liu, Y. Zhu, T. Zeng, Y. Zhao, R. Chen and B. Shan, *Catal. Sci. Technol.*, 2018, **8**, 5490-5497.
17. J. S. Elias, K. A. Stoerzinger, W. T. Hong, M. Risch, L. Giordano, A. N. Mansour and Y. Shao-Horn, *ACS Catalysis*, 2017, **7**, 6843-6857.
18. C. Ma, C. Yang, B. Wang, C. Chen, F. Wang, X. Yao and M. Song, *Appl. Catal. B: Environ.*, 2019, **254**, 76-85.
19. X.-m. Zhang, Y.-Q. Deng, P. Tian, H.-h. Shang, J. Xu and Y.-F. Han, *Appl. Catal. B: Environ.*, 2016, **191**, 179-191.